Collaborative strengthening by multi-functional molecule 3-thiophenboric acid for efficient and stable planar perovskite solar cells

Yuanxin Zhong [a],[1], Chunmei Li [a],[1], Gaobo Xu [a],[1], Cunyun Xu [a], Jun Dong [a],[b], Dingyu Liu [a], Dengcheng Lu [a], Jiayu You [a], Chunming Gao [c],[*], Qunliang Song [a],[*]

[a] *Institute for Clean Energy and Advanced Materials, School of Materials and Energy, Southwest University, Chongqing Key Laboratory for Advanced Materials and Technologies of Clean Energy, Chongqing 400715, PR China*
[b] *Key Laboratory of Extraordinary Bond Engineering and Advance Materials Technology (EBEAM) of Chongqing, Yangtze Normal University, Chongqing 408100, PR China*
[c] *School of Optoelectronic Science and Engineering, University of Electronic Science and Technology of China, Chengdu 610054, PR China*

A B S T R A C T

Drawbacks like serious interface defects, imperfect energy level arrangement and uncontrollable perovskite nucleation hinder further improvement to achieve efficient and stable planar perovskite sollar cells (PSCs), which fortunately can be solved by interface modification with small molecules. However, it is still a challenge to develop more simple and efficient multi-functional small molecules to simultaneously solve these problems. Herein, conjugated small molecule 3-thiophenboric acid (TBA) was utilized for the first time at the SnO_2/ perovskite interface to achieve this goal. With the dipole moment of TBA, the energy level arrangement between SnO_2 and perovskite is optimized. Defects at both sides of the interface are passivated by functional groups on TBA effectively, inhibiting the non-radiative recombination and reducing the energy loss. Besides, the quality of perovskite film is improved due to inhibited disordered heterogeneous nucleation. As a result, the open voltage (V_{OC}), short current density (J_{SC}) and fill factor (FF) are all improved, which leads to a champion device with PCE up to 21.80%, much higher than 19.74% of control one. In addition, our optimized devices show excellent stability when storing for a long time, aging under high humidity and under continuous illumination. Our results provide a novel strategy to improve the efficiency and stability of PSCs synergistically by multi-functional conjugated small molecule.

1. Introduction

With sufficient research background, organic–inorganic hybrid perovskite solar cells (PSCs) have shown remarkable efficiency growth in the last decade (3.8% in 2009 to 25.5% at present) [1–5]. It not only comes from the excellent properties of hybrid perovskite, such as tunable optical band gap [6,7], long carrier diffusion length [8] and high light absorption coefficient [9], but also depends on the technical progresses like new fabrication approaches [10–13], composition engineering [14], interface engineering [15] and so on. Such high photoelectric conversion efficiency (PCE) also indicates that PSCs have great potential to compete with conventional crystalline silicon solar cells in the future market.

Compared to the p-i-n structure, devices with n-i-p structure have attracted much attention due to their high efficiency. The high efficiency can vastly ascribe to the electron transport material (ETM), which is applied to extract electrons efficiently, block holes and even provide a good substrate for perovskite film growth [16–18]. Recently, SnO_2 has been developed as a promising alternative ETM among the commonly used ones including titanium dioxide (TiO_2) [19], zinc oxide (ZnO) [20] and tin dioxide (SnO_2) in n-i-p devices [21]. With the excellent properties of SnO_2 such as high bulk electron mobility (240 cm^2 V^{-1} s^{-1}) [22], weak UV photocatalytic activity [23] and low temperature preparability (<200 ℃) [24], the certified PCE of PSCs based on SnO_2 electron transport layer (ETL) has exceeded 25% [25], implying the great potential of SnO_2. Among the common preparation methods of SnO_2 layer such as solution process, atomic layer deposition (ALD) [26], chemical bath deposition (CBD) [25] and so on, the solution process is

the most convenient and efficient. You *et al.* achieved a certified efficiency of 19.9% and reduced hysteresis using commercial SnO$_2$ aqueous colloidal precursor for spin-coating [27]. Similarly, Han *et al.* prepared a uniform and pinhole-free SnO$_2$ layer with a large area using the same commercial colloidal dispersion [28]. However, there are still some drawbacks in the PSCs based on SnO$_2$ ETL. The imperfect energy level arrangement between SnO$_2$ and perovskite may cause unnecessary energy loss and charge accumulation at interface, which brings about low V_{OC} and obvious hysteresis [29,30]. Like other metal oxide, large amounts of adsorbed hydroxyl groups on the surface of SnO$_2$ ETL caused by thermal annealing at ~ 150 ℃ always generate defects at the interface, which deteriorate the device performance by serious non-radiative recombination [31–33]. The ionic property of perovskite easily leads to under-coordinated halides and lead ions at the interface, mainly forming Pb^{2+}. These ion vacancies not only cause the collapse of the perovskite crystal structure but also become recombination centers at the interface [34–36]. In addition, lattice mismatch between SnO$_2$ and perovskite may leads to poor contact, which results in interfacial states, stresses, uncontrolled nucleation and growth of perovskite [31,37].

Interface engineering, especially using small molecule with better controllability than polymer materials, is an effective way to optimize energy level alignment, eliminate the undesirable defects, improve contact properties and promote perovskite crystallization [38–41]. Hou *et al.* used dopamine self-assembly layer to modify the SnO$_2$ surface, which promoted the crystallization and growth of perovskite by improving the wettability of SnO$_2$ ETL, so as to mainly enhance short-circuit current (J_{SC}) [42]. The 4-imidazoleacetic acid hydrochloride was reported by Park *et al.* to provide a chemical bridge at the interface of SnO$_2$ and perovskite, which improved the crystallinity of perovskite film, passivated defects and optimized energy level alignment. Unfortunately, only increase of open-circuit voltage (V_{OC}) from 1.08 to 1.14 V was achieved with almost no increase of J_{SC} [43]. Recently, a PCE of 21.23% benefited from enhanced V_{OC} (from 1.114 to 1.164 V) and improved device stability were achieved by using BPTC-BN to passivate defects at SnO$_2$/perovskite interface and improve the morphology of perovskite film. Nevertheless, again, current increase was not reported [44]. Yuan *et al.* reported the NbO$_x$ modified SnO$_2$ NPs as efficient ETMs for planar PSCs and achieved a high PCE up to 24.01% due to the passivation of interface defects as well as improvement of the crystallinity of perovskite films [45]. Moreover, Padture *et al.* used an iodine-terminated self-assembled monolayer (I-SAM) to increase the interface adhesion toughness between the SnO$_2$ and perovskite film and reduce the hydroxyl groups number on the SnO$_2$ surface, which resulted in improved voltage and stability [31]. Our previous work also shown that zwitterion, DETAPMP, can be used to link SnO$_2$ with perovskite and a significant enhanced J_{SC} and cell stability were obtained by defect passivation [46]. From the modification procedures above, the molecule we choose should have at least two contrapuntal functional groups at the same time. One can reacts with the groups on SnO$_2$ surface to facilitate molecular arrangement and defect passivation, and the other coordinates with the defect in perovskite to achieve bridging at the interface. However, it is still a challenge to develop simple and efficient multi-functional small molecules to achieve comprehensive enhancements of device performance via the collaborative optimization of 1) energy level arrangement, 2) interface defect passivation and 3) perovskite crystallization.

In this work, we devised a simple and effective method by inserting a conjugated small molecule 3-thiophenboric acid (TBA) between the SnO$_2$ ETL and perovskite. Density functional theory (DFT) calculations, X-ray photoelectron spectroscopy (XPS) and Fourier transform infrared spectroscopy (FTIR) were performed to study the mechanism of this modification. Carrier dynamics, interfacial band structure, defect states and morphology were systematically demonstrated by a series of optical and electrical characterization methods to explore the roles of TBA. The results show that the energy level arrangement between SnO$_2$ and perovskite can be improved due to the dipole effect of TBA. The number of absorbed –OH groups on SnO$_2$ surface is reduced through esterification and the S atom with lone pair electrons in thiophene ring can cooperate with uncoordinated Pb^{2+} at the lower surface of perovskite layer. Thus, the electron extraction from perovskite to SnO$_2$ is greatly enhanced with less energy loss and defects at the interface are reduced which leads to inhibition of non-radiative recombination. Besides, the thiophene rings on TBA molecules also provide controllable nucleation sites for perovskite growth and non-wetting substrate to inhibit disordered heterogeneous nucleation, thus good film quality, less pin-holes and reduced defects of perovskite are achieved. Therefore, the dipole structure and different functional groups of TBA molecules can realize multiple functions including (1) optimizing the interface energy level arrangement, (2) passivating the defects at both sides of the interface, (3) improving the quality of perovskite film. Thanks to the cooperation of TBA, we achieved the comprehensive improvement of J_{SC} (from 21.662 to 22.301 mA cm^{-2}), V_{OC} (from 1.138 to 1.179 V) and FF (from 78.56% to 79.92%). Finally, the PSC based on SnO$_2$/TBA ETL achieved a high PCE of 21.80% with almost no hysteresis, contrast to 19.74% of control one without TBA modification. At the same time, our optimized devices shown better stability at the humidity of ~ 20% RH, ~50% RH and under continuous illumination due to the reduction of interface defects and optimization of perovskite film. The unencapsulated device with TBA treated SnO$_2$ retained near 90% of its initial PCE after aging for 1000 h at ~ 20% RH.

2. Experimental section

2.1. Materials

Etched indium tin oxide (ITO) substrates (sheet resistance of 7 ~ 9 Ω/sq) were purchased from Advanced Election Technology Co., Ltd.. The SnO$_2$ colloidal dispersion was obtained from Alfa Aesar. Lead (II) bromide (PbBr$_2$, 99.99%). Methylammonium bromide (MABr, 99.5%), Methylammonium chloride (MACl, 99.5%), Spiro-OMeTAD (99.5%) and LiTFSI (99%) were purchased from Xi'an Polymer Light Technology Corp. Formamidine Hydroiodide (FAI, 99.9%), lead(II) iodide (PbI$_2$, 99.99%) were obtained from Advanced Election Technology Co., Ltd.. N,N-Dimethylformamide (DMF, 99.9%), dimethyl sulfoxide (DMSO, 99.9%) and isopropanol (IPA, 99.5%) were purchased from J&K Scientific Ltd.. Chlorobenzene (CB, 99.8%) was obtained from Shanghai Meryer. 4-Tert-Butylpyridine (TBP, 96%) was obtained from Sigma Aldrich, and 3-thiophenboric acid (TBA, 99.95%) was purchased from Shanghai bidepharm Technology Co., Ltd.. All the materials were used as received unless specified.

2.2. Device fabrication

ITO glass was cleaned for several times with detergent and deionized water in an ultrasonic cleaning machine (KQ3200DV), and then blew with dry N$_2$. The SnO$_2$ colloidal dispersion (15% in H$_2$O colloidal dispersion) was diluted to 3.75% with deionized water, and then 40 μL of the diluted dispersion was spin coated on the ITO substrate at 4000 rpm for 40 s and then annealed at 150 °C for 30 min in ambient environment to form a dense SnO$_2$ film. After cooling down to room temperature, the substrates were transferred into a glove box. For the TBA-treated devices, the TBA solution (0.5, 1, 2, 6 mg mL^{-1}) were spin coated on the SnO$_2$ at 4000 rpm for 30 s and then annealed at 100 °C for another 5 min to remove excess solvent. After cooling down to room temperature, the substrates were washed with 150 μL isopropanol to remove the dissociative TBA molecules. The (FAPbI$_3$)$_{0.93}$(MAPbBr$_3$)$_{0.07}$ perovskite precursor was prepared by dissolving 645.4 mg PbI$_2$, 240.5 mg FAI, 12.2 mg MABr, 40.4 mg PbBr$_2$ and 34 mg MACl in 1 mL mixed solvent (DMF:DMSO = 8:1), followed by stirring for 2 h at room temperature. The dense perovskite film was prepared by spin coating 40 μL precursor solution on the substrate at 3500 rpm for 30 s. After reaching maximum speed, 80 μL CB was dropped at 13 s before the end, then the

intermediate film was transferred to the 130 ℃ hot plate and annealed for 30 min. The doped Spiro-OMeTAD solution was prepared by dissolving 50 mg Spiro-OMeTAD, 12.5 μL LiTFSI (520 mg mL^{-1} in acetonitrile) and 20.4 μL TBP in 1 mL CB, then stirring for 2 h to mix completely. The HTL was prepared by spin coating doped Spiro-OMeTAD solution on the perovskite film at 4000 rpm for 30 s and no annealing followed. Finally, 120 nm of Ag were thermally evaporated on top of the HTM layer to obtain a complete device with an effective area of 0.06 cm^2.

2.3. Characterizations

Current-voltage (*J-V*) curves were measured using a solar simulator and a Keithley 2400 source meter. Light intensity was adjusted to AM 1.5G (100 mW cm^{-2}) with an calibrated Si solar cell. The test range was + 1.2 to −0.2 V (reverse scan.) or −0.2 to + 1.2 V (forward scan), the 0.02 V step was set. Incident photon-to-electron conversion efficiency (IPCE) was tested using xenon lamp (Newport, 69920) as light source. The photocurrents from the device or the calibrated silicon detector were measured by a lock-in amplifier (SR-830) to calculate the light intensity and then the IPCE. The electrochemical impedance spectroscopy (EIS) was measured with an electrochemical workstation (CHI 660D) in the frequency range of 3 Hz-100 kHz. The bias potential was 1.0 V with amplitude of 20 mV under AM 1.5G simulated light. UV–Vis absorption spectra were obtained by a UV–Vis spectrometer (Shimadzu UV-21011C). The steady-state photoluminescence (PL) spectra were taken on an FLSP920 and the time-resolved photoluminescence (TRPL) were measured with an FLS 1000 spectrometer. The XPS and UPS were obtained by Thermo Fisher ESCALAB 250Xi. The X-ray diffraction patterns were carried out by an XRD-7000 X-ray diffractometer from SHIMADZU. The surface and cross-sectional morphology of perovskite films were measured by field-emission scanning electron microscopy (SEM,

JSM-6700F). The EDS spectra were obtained using the same system. The surface roughness was obtained using atomic force microscopy (AFM CSPM 5500). The contact angle goniometer (YIKE-360A, Chengde Precision Test Instrument Factory, China) was employed to test the contact angle (CA). The thickness of perovskite films were measured by a step profiler (KOSAKA, ET-150). Transient photovoltage (TPV) and transient photocurrent (TPC) of devices were measured by laser pulses (532 nm, 6 ns width from an Nd:YAG laser) with input impedance of 1 MΩ/50 Ω. The FTIR spectra were recorded with a Nicolet iS50 Infrared Fourier transform microscope by Thermo Fisher Nicolet 6700.

3. Results and discussion

The configuration of control device is ITO/SnO$_2$/(FAPbI$_3$)$_{0.93}$(MAPbBr$_3$)$_{0.07}$/Spiro-OMeTAD/Ag, as shown in Fig. 1**a**. The TBA modifier is inserted between SnO$_2$ and perovskite (PVSK) layers. The TBA is a conjugated molecule composed of functional groups including thiophene ring and hydroxyls. The fabrication procedure of the TBA layer is shown in **Fig. S1** and the cross-sectional SEM image of PSC is shown in **Fig. S2**.

Before verifying the effect of TBA at the interface by experiments, the density functional theory (DFT) calculations were performed to make predictions in advance. The computational details are shown in Supplementary Material. The structure with electrostatic potential (ESP) map of TBA molecule is shown in **Fig. S3**, from which the charge distribution of the molecule can be seen [47]. The color gradient from yellow to red indicates an increase in electrostatic potential from borate group to thiophene ring, which suggests that TBA molecule has dipole moment and can link SnO$_2$ and PVSK. The calculation results show that the hydrogen (H1) on the hydroxyl group near the S atom is more easily to ionize, while the bond strength of O-H1 bond is only 0.028 eV lower than the another O-H2 bond. Subsequently, considering these two forms
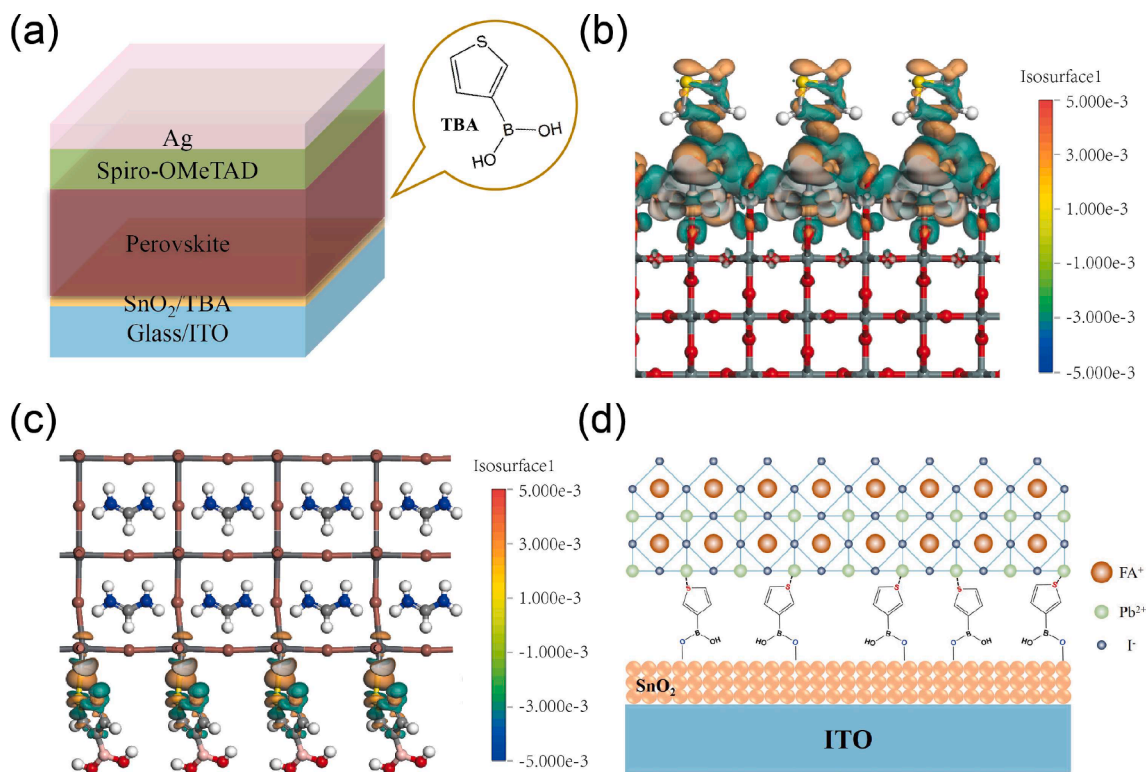
Fig. 1. (a) Schematic structure of PSC based on SnO$_2$/TBA ETL. (b and c) Graphic structures with electron density difference plots of (b) SnO$_2$ (1 1 0) surface with adsorbed TBA molecules bonded with the borate group in TBA (c) (0 0 1) surface of PbI$_2$-terminated α-FAPbI$_3$ with adsorbed TBA molecules bonded with the thiophene ring in TBA (the isosurface value is set as 0.003 e Å^{-3}). The orange color indicates electron gain and the green part suggests electron loss. (d) Interaction diagram of TBA molecules with SnO$_2$ and perovskite.

of ionization, the interaction between the SnO$_2$ surface and TBA molecules were investigated. SnO$_2$ (1 1 0) surface with the lowest surface energy was selected as the model here [48] and the dangling bonds of Sn atoms at the surface promote the adsorption of bridged oxygen and –OH groups as shown in **Fig. S4a**. Different binding atoms and adsorption orientations of TBA molecules on SnO$_2$ surface were considered, and the most stable adsorption form was determined as shown in Fig. 1**b**. The obtained electron density difference plots in Fig. 1**b** indicates that the borate group in TBA could react with the absorbed –OH groups on SnO$_2$ surface by esterification to form Sn-O-B bond. Orange and green colors represent electron gain or loss respectively. The significant charge transfer at the interface implies the bonding interaction between TBA molecule and SnO$_2$ matrix. The electron exchange is concentrated between O and Sn atoms at the interface and decreases away from the interface, indicating the ionic binding interaction between TBA molecule and SnO$_2$ matrix. Once it was confirmed that TBA could be adsorbed stably on the surface of SnO$_2$, we further studied the interaction between TBA and perovskite on this basis (Fig. 1**c**), where the PbI$_2$-terminated α-FAPbI$_3$ (0 0 1) surface with low surface energy is chosen as growth plane [31]. It can be seen that the S atom in the thiophene ring of TBA molecule could interacts with Pb^{2+} on the perovskite surface obviously. The electron absorption characteristic of S atom is beneficial to obtain electrons from uncoordinated Pb^{2+} (electron donor) on the perovskite surface. However, O atoms also have lone pair electrons that have the opportunity to coordinate with Pb^{2+}, therefore it is important to exclude the interaction between borate group and perovskite. In order to answer this question, we simulated and calculated the interaction between thiophene ring and SnO$_2$ (1 1 0) surface. Only under the premise that the thiophene ring can bond with SnO$_2$, anchoring TBA molecules and exposing the borate group on the top, can the O atom in the borate group have a chance to react with the perovskite. As shown in **Fig. S4b and S4c**, however, it is difficult for thiophene ring to react with SnO$_2$ surface because S atom cannot bond with the surface atoms and no stable anchoring site was found (the elliptical parts indicate the

distances between S atom and the nearest surface O atoms which fail to bond). Thus, we believe that the –OH in TBA can interact with the hydroxyl group adsorbed on Sn atom, forming Sn-O-B bond through releasing H$_2$O. This linkage between TBA and SnO$_2$ thus reduces the hydroxyl groups adsorbed on the surface. The simulated interaction mechanism is shown in Fig. 1**d**. Besides, there are two hydroxide groups in TBA, thus we investigated the interactions between each hydroxide group in TBA and SnO$_2$ surface respectively. The results show that both of the two hydroxide groups can react with absorbed –OH on SnO$_2$ surface, sticking TBA molecules on the surface (**Fig. S5a and S5b**). The exposed thiophene rings can provide S atoms coordinating with Pb^{2+} in perovskite, as shown in electron density difference plots (**Fig. S5c-f**).

To further determine the interaction mechanism between TBA and SnO$_2$ as well as perovskite under experimental conditions and verify the results of DFT calculation, the XPS measurements were carried out [49]. Here we studied the interaction between TBA and perovskite by coating TBA on the prepared perovskite film. The XPS survey spectra of pristine SnO$_2$, TBA-modified SnO$_2$, pristine perovskite and TBA-modified perovskite films are shown in **Fig. S6a and S6b**. As illustrated in Fig. 2**a and 2b**, the B 1 s and S 2p spectra confirm the presence of TBA molecules on the surface of SnO$_2$ after solvent washing, which is further affirmed in the EDS map of SnO$_2$/TBA film (**Fig. S7**). Fig. 2**c** shows that the binding energy of Sn 3d$_{3/2}$ (494.76 eV) and Sn 3d$_{5/2}$ (486.37 eV) for pristine SnO$_2$ shift to 495.01 and 486.61 eV respectively after TBA modification. This indicates a strong interaction between TBA and SnO$_2$ to change the electron cloud density around the Sn atoms, which is consistent with the DFT calculation results [43]. At the same time, interaction between TBA and perovskite is also confirmed by the shift of Pb 4f$_{5/2}$ and Pb 4f$_{7/2}$ peaks from 143.00 and 138.14 eV to higher 143.09 and 138.23 eV (Fig. 2**d**). According to the DFT calculation results, in-depth analysis of the O 1 s spectra of the SnO$_2$ and TBA modified SnO$_2$ films is critical to understand the interaction between TBA and SnO$_2$. Therefore, the XPS spectra of O 1 s were measured and the peak fitting is carried out in Fig. 2**e and 2f**. The O 1 s spectra of pristine SnO$_2$
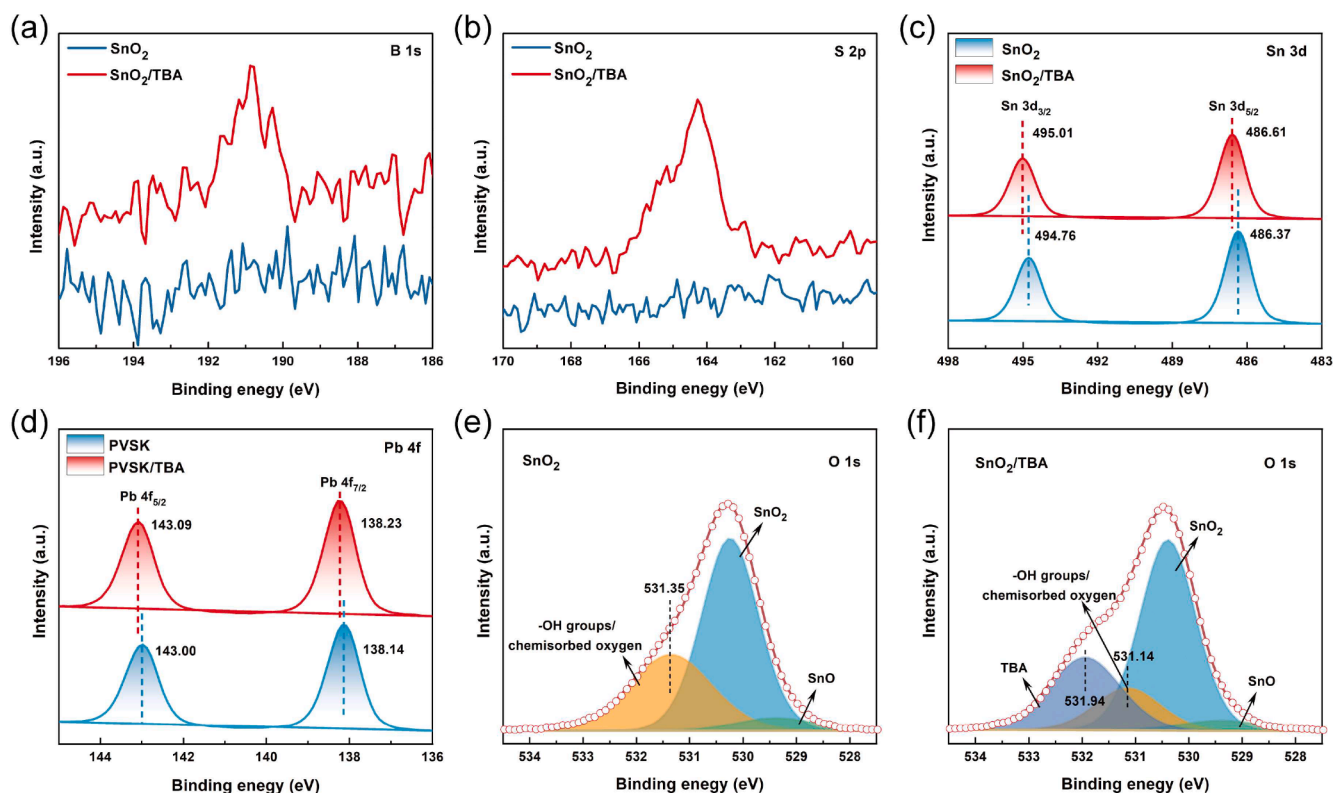

Fig. 2. XPS spectra of (a) B 1 s, (b) S 2p and (c) Sn 3d for SnO$_2$ films with and without TBA modification. (d) Pb 4f spectra of the perovskite with and without TBA coating. O 1 s spectra of (e) the pristine SnO$_2$ film and (f) the SnO$_2$/TBA film.

film can be divided into three peaks. The peak at about 530.26 eV (blue) is assigned to the lattice oxygen from SnO_2, the peak located at 529.38 eV (green) is attributed to the lattice oxygen from SnO and the peak at higher binding energy (531.35 eV, yellow) is classified as surface chemisorbed oxygen which are mainly –OH groups [46]. Obviously, after TBA treatment, an obvious asymmetric broad peak appears at the higher binding. Peak fitting shows that the lattice oxygen (SnO_2 and

SnO) does not change significantly, but a new oxygen specie appears at 531.94 eV, which is belong to the redundant –OH groups in TBA molecules. More importantly, the peak of –OH adsorbed on the SnO_2 film moves to lower binding energy of 531.14 eV and the intensity is greatly suppressed. This observation confirms the results of DFT calculation that the borate in TBA molecule can interact with the –OH on the surface of SnO_2 film by esterification to form Sn-O-B bond and reduce the amount
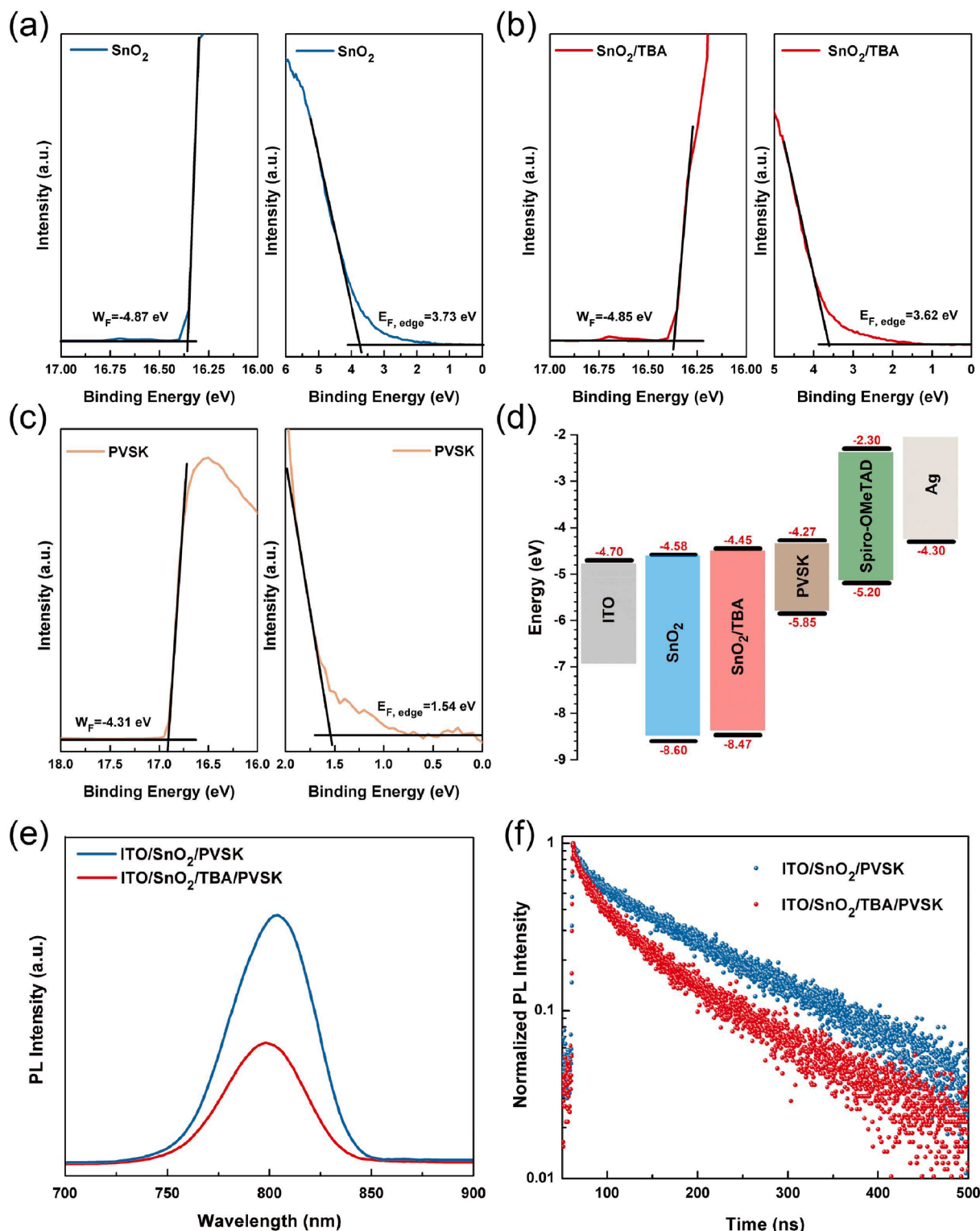
Fig. 3. The UPS spectra of (a) pristine SnO_2, (b) SnO_2/TBA and (c) perovskite films. (d) Energy level diagram of different layers in device. Steady-state (e) and time-resolved PL (f) spectra of the perovskite films based on bare SnO_2 and TBA modified SnO_2 substrates.

of –OH groups. Furthermore, the interaction between TBA and SnO_2 as well as perovskite were also confirmed by FTIR spectra (**Fig. S8**). It's worth noting that to easier distinguish the signal, the method of powder mixture grinding (TBA and SnO_2 or PbI_2) was used. In **Fig. S8a**, the stretching vibration peak of O–H of absorbed –OH on SnO_2 sample appears at 3431.4 cm^{-1} and the O–H in the TBA molecule appears at 3274.1 cm^{-1}. The broadened peak of O–H indicates the interaction between the borate in TBA and the –OH absorbed on SnO_2. Moreover, this effect is also reflected in the B-O stretching vibration peak shifting from 1415.7 cm^{-1} of TBA molecule to 1402.8 cm^{-1} of SnO_2-TBA mixture (**Fig. S8b**), confirming the XPS results. As illustrated in **Fig. S8d**, after reacting with PbI_2, the peak of C-S-C in TBA (1027.4 cm^{-1}) shifts to 1042 cm^{-1}. In combination with the shifted Pb 4f peaks in **Fig. 2d** and the DFT calculation, we can conclude that the S atoms in thiophene groups are easy to coordinate with Pb^{2+} in perovskite.

The ultraviolet photoelectron spectroscopy (UPS) was performed firstly to explore the effect of TBA on the energy level arrangement as shown in **Fig. 3a-c**. The cut-off binding energies ($E_{cut-off}$) of SnO_2 and SnO_2/TBA are 16.35 and 16.37 eV respectively. According to equation $E_F = E_{cut-off}-21.22$ eV, the calculated Fermi level (E_F) of SnO_2 and SnO_2/TBA are −4.87 and −4.85 eV respectively. The Fermi edge ($E_{F, edge}$) is estimated to be 3.73 eV for SnO_2 and 3.62 eV for SnO_2/TBA. The valence band energy level (E_{VB}) of SnO_2 and SnO_2/TBA films are calculated as −8.6 and −8.47 eV respectively using the formula $E_{VB} = E_F-E_{F, edge}$. Finally, according to the measured optical band gap value of 4.02 eV (**Fig. S10**), the conduction band energy level E_{CB} are calculated to be −4.58 eV for SnO_2 and −4.45 eV for SnO_2/TBA. Similarly, the E_F, E_{VB} and E_{CB} of the perovskite film are calculated to be −4.31, −5.85 and −4.27 eV respectively (**Fig. S11**). Fig. 3d shows the energy level alignment diagram of the device. Compared with pristine SnO_2, the E_{CB} and E_F of SnO_2/TBA film shift upward slightly and are closer to the E_{CB} and E_F of perovskite film. Our DFT calculation indicates ordered dipoles are formed after TBA modification, which are believed to be the reason of the energy shift [43]. Such better energy level arrangement is beneficial for the electron extraction at the interface and reduction of energy loss, which may leads to less hysteresis and higher V_{OC} of devices as discussed below.

Subsequently, for the better understanding of carrier dynamics at the interface, steady-state PL and time-resolved PL (TRPL) spectra were measured for perovskite films deposited on SnO_2 and TBA modified SnO_2. As shown in **Fig. 3e**, more PL quenching is observed in the perovskite film grown on SnO_2/TBA substrate. The increased PL quenching may be due to 1) the enhancement of electron extraction and transportation at the interface, 2) the more trap-states caused by inferior perovskite film. The SEM image of perovskite film deposited on SnO_2/TBA substrate shows less pin-holes than film based on SnO_2 ETL (**Fig. S12a and S12c**), which is beneficial for carrier transportation and long-term stability. Moreover, the vertically oriented grains across the whole SnO_2/TBA based perovskite film also exclude the more traps in the film (**Fig. S12b and S12d**). The better crystallization and growth of perovskite can be ascribed to the inhibited disordered heterogeneous nucleation by TBA, which mainly comes from the increased contact angle (CA) of substrate (**Fig. S14c and S14d**) and is confirmed by the results of XRD intensity and light absorption enhancement of perovskite (**Fig. S12e and S12f**). The interface defect passivation also contributes to the inhibition of non-radiative recombination. All these positive information come to beneficial effect of TBA modification. Thus, the PL quenching is associated with the interface change rather than the perovskite film. We determine that PL quenching comes from a more matched energy level alignment, which improves the charge transfer at the interface. To further quantify the carrier lifetime, TRPL spectra of perovskite films based on different substrates were tested (**Fig. 3f**). By fitting the corresponding curves with bi-exponent decay function, the fast and slow decay lifetime (τ_1 and τ_2) and calculated average decay lifetime (τ_{ave}) were obtained (**Table S2**) [44]. The lower τ_{ave} of the perovskite film deposited on TBA-modified SnO_2 (97.44 ns) compared to

that of the original one (148.61 ns) is consistent with the PL results, which means better charge transfer happened at interface.

To evaluate the defects, the space-charge-limited current (SCLC) was firstly tested [50]. As shown in Fig. 4a and 4b, the dark *J-V* curves of the electron-only devices can be divided into three parts: the Ohmic region, trap-filling limited region with a sharp increase in current and the trap-free Child's region. Here, V_{TFL} decreases from 0.436 to 0.269 V after TBA modification and then the trap density (N_t) of perovskite films are calculated by the equation [51]:

$$N_t = \frac{2V_{TFL}\varepsilon_r\varepsilon_0}{qL^2} \tag{1}$$

where ε_r is the relative dielectric constant of perovskite, here 30.8 is chosen [43], ε_0 is vacuum dielectric constant, q is electric charge and L is the thickness of perovskite film (~600 nm as shown in **Fig. S9**). The calculated N_t decreases significantly from 4.12×10^{15} to 2.54×10^{15} cm^{-3} after TBA modification (**Table S3**). According to the results mentioned above, the reduction of defects in perovskite film can be mainly attributed to the coordination of S atoms in TBA with Pb^{2+} in perovskite. Moreover, the improvement of perovskite crystal quality and the reduction of pin-holes also have some contributions to the decrease of defects. Then, the EIS were performed in the frequency range of 3 Hz-1000 kHz under AM 1.5G simulated light to obtain deep insight into interfacial charge transfer and recombination (**Fig. 4c**). The bias potential is 1.0 V with an amplitude of 0.02 V. The fitted EIS spectra results are listed in **Table S4**. The semicircle in the low frequency region represents the recombination resistance (R_{rec}), indicating the degree of non-radiative recombination at the interface. The semicircle in the high frequency range represents the transport resistance (R_{tr}), indicating the charge transfer and interfacial charge extraction in the device [52]. After TBA modification, the R_{tr} decreases from 266.5 to 183.5 Ω, suggesting the improved charge transfer and better extraction at SnO_2/perovskite interface, which is consistent with the UPS results. The R_{rec} increases from 154.0 to 266.3 Ω, implying the effective defect suppression by TBA modification. The reduction of defects comes from the decrease of –OH groups on SnO_2 surface by esterification and coordination between S atoms in TBA and Pb^{2+} in perovskite, which can be verified by the decreased ideality factor (n). As shown in **Fig. 4d**, the n values decrease from 1.70 to 1.52 kT/q for PSCs based on SnO_2 and SnO_2/TBA ETLs. Finally, the TPC and TPV were performed to study the carrier transport process, carrier lifetime and recombination rate in PSCs [53]. As shown in **Fig. 4e and 4f**, compared with the control device, the TPC of the device based on SnO_2/TBA ETL decays faster, indicating its better carrier transport. Moreover, the TPV decays more slowly after TBA modification, implying a longer carrier lifetime, which related to less non-radiative interfacial recombination. In a word, TBA modification can passivate the interface defects by removing surface hydroxyl groups and coordinating with Pb^{2+}, improve the crystallization and growth of perovskite, and reduce the bulk defects. Therefore, faster carrier transport and longer carrier lifetime are achieved.

The positive effects of TBA molecule on defect passivation, energy level adjustment, carrier dynamics and perovskite crystallization in PSCs can definitely influence the device performance. As illustrated in **Fig. S15** and **Table S5**, the optimization TBA concentration was obtained as 1.0 mg mL^{-1}. In addition, as shown in **Fig. S16**, we excluded the contribution of solvent IPA. The efficiency drop after 1 mg mL^{-1} is mainly due to the insulating property of TBA, which is mainly reflected in the conductivity decrease of the SnO_2/TBA film when using higher concentrated TBA, as shown in **Fig. S17**. After optimization, the average V_{OC}, J_{SC}, FF and PCE increase from 1.138 V, 21.662 mA cm^{-2}, 78.56% and 19.32% of the control devices to 1.179 V, 22.301 mA cm^{-2}, 79.92% and 21.01% of the 1.0 mL^{-1} TBA modified devices. The champion devices are compared in the **Fig. 5a**. The higher PCE up to 21.80% compared to the control one (19.74%) is attributed to the comprehensive improvement of V_{OC} (from 1.163 to 1.197 V), J_{SC} (from 21.895 to 22.526 mA cm^{-2}) and FF (from 77.51% to 80.83%). Furthermore, the
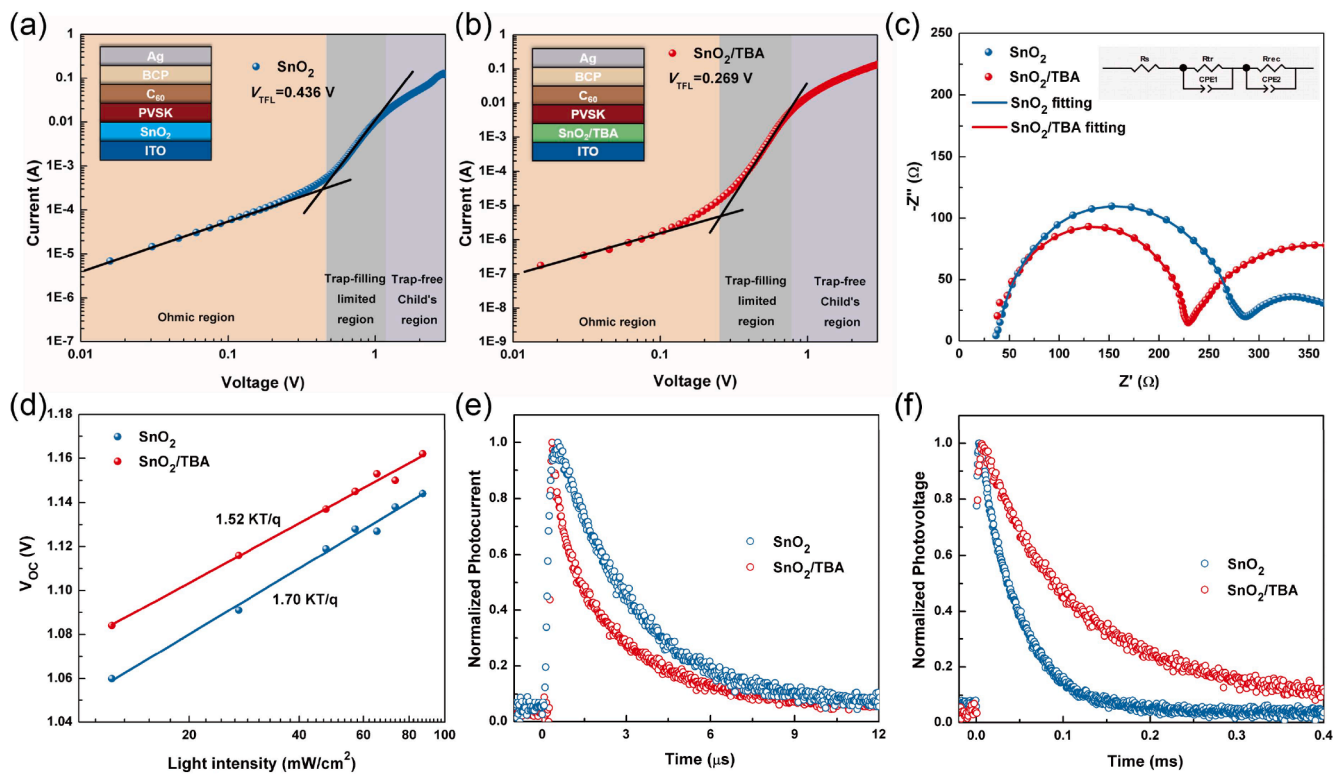
Fig. 4. Dark *J-V* curves of electron-only (ITO/ETL/PVSK/C$_{60}$/BCP/Ag) devices (a) without or (b) with TBA treatment. (c) Nyquist plots and the equivalent circuit. (d) Open circuit voltage values of the PSCs with/without TBA treatment as function of light intensity. (e) TPC and (f) TPV of the devices based on SnO$_2$ or SnO$_2$/TBA ETLs.
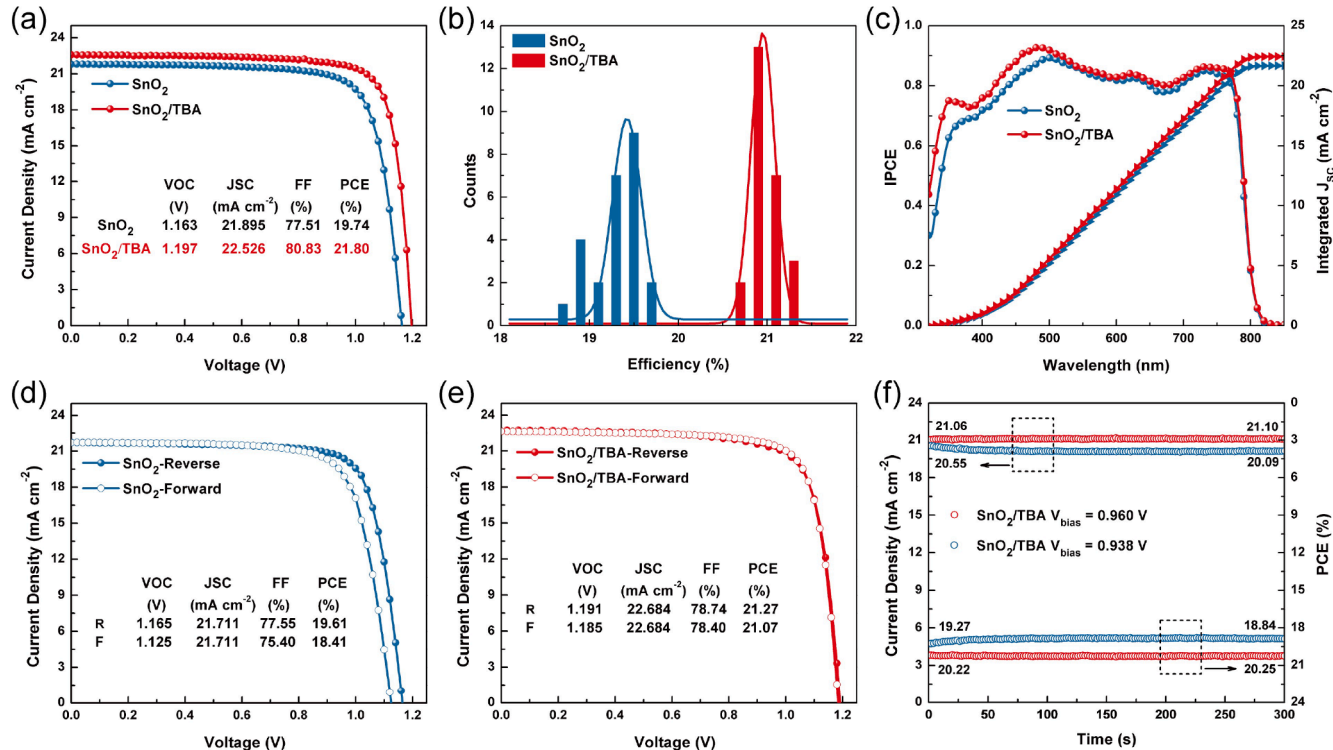

Fig. 5. (a) The *J-V* curves of the champion devices based on pristine SnO$_2$ or SnO$_2$/TBA ETLs. (b) Statistical PCE distribution of the pristine and TBA modified PSCs. (c) IPCE and corresponding integrated current curves of devices based on SnO$_2$ or SnO$_2$/TBA ETLs. (d, e) *J-V* curves measured by reverse scan (RS) and forward scan (FS), (f) Stabilized output current densities and efficiencies at maximum power points for control and TBA optimized PSCs.

PSCs based on the SnO_2/TBA ETL have excellent reproducibility as shown in the Fig. 5b. The increase in V_{OC} is attributed to the better energy level alignment and passivation of defects at SnO_2/perovskite interface including the reduction of hydroxyl groups on SnO_2 surface and coordination of Pb^{2+} in perovskite. The increase of J_{SC} is mainly comes from the optimized perovskite crystallization that leads to better light absorption as UV–Vis results shown and the improved carrier transport, and the increased conductivity of SnO_2/TBA film (Fig. S17) mainly responsible for FF enhancement.

Fig. 5c shows the IPCE spectra of the control and optimized devices. The integrated current density increases from 21.672 to 22.441 mA cm^{-2}, consisting with the trend of *J-V* curves. Moreover, the PSC after TBA modification show weaker hysteresis (hysteresis index, HI = 0.009) than the control one (HI = 0.06) (Fig. 5d, 5e and Table S6), suggesting the less charge accumulation at SnO_2/TBA interface. Furthermore, we tested the stable output for 300 s at maximum power point of the control and optimized devices (Fig. 5f). After 300 s, the current density and PCE of the control device decrease from 20.55 mA cm^{-2} and 19.27% to 20.09 mA cm^{-2} and 18.84%, respectively. In contrast, the performance of TBA-modified device is very stable during the same period of time.

In the end, we stored the unencapsulated devices in ambient at ~ 20% RH and tested their performance ocassionally for more than 1000 h to investigate their stability. As shown in Fig. 6. only 35% of the initial PCE is maintained for the control device after 1000 h storage, contrast to the about 90% PCE for the device based on SnO_2/TBA ETL. The stability evaluations have also been conducted under ambient humidity (~50% RH) for 200 h (Fig. S18) and under continious illumination (Fig. S19). Though the decay rate are different, all tests show the better stability of

devices after TBA modification, showing the same trend in Fig. 6. The longer lifetime is mainly due to the stability of TBA molecule itself, the reduction of interface defects under the multiple passivation by TBA modification and the pin-hole free perovskite film from optimization of crystallization. All are beneficial to the device structure stability and reduction of water/oxygen penetration and ion migration.

4. Conclusion

In summary, we have successfully developed a multi-functional conjugated molecule TBA to modify the interface between SnO_2 ETL and perovskite. The interaction between TBA and SnO_2 as well as perovskite was simulated by DFT calculation, and was verified by XPS and FTIR spectra. TBA molecules can stick to the surface of SnO_2 through the esterification reaction between borate and hydroxyl group absorbed on the SnO_2, forming B-O-Sn bonds to reduce the number of hydroxyl groups. The S atoms in thiophene groups of TBA provides electrons and coordinate with lead ions in perovskite. Moreover, TBA also provides the nucleation sites and less hydrophilic substrate for perovskite growth. After TBA modification, the better energy level arrangement reduces the energy loss thanks to the dipole moment of TBA. The defects of SnO_2/perovskite interface are reduced and the trap-assisted non-radiative recombination are suppressed. Furthermore, the quality of perovskite film is improved thanks to less pin-holes and harmful grain boundaries. In the end, we achieved a comprehensive improvement, leading to PCE increase from 19.74% to 21.80% with improved stability. The unencapsulated device based on TBA treated SnO_2 retained about 90% of its initial efficiency after aging for 1000 h in
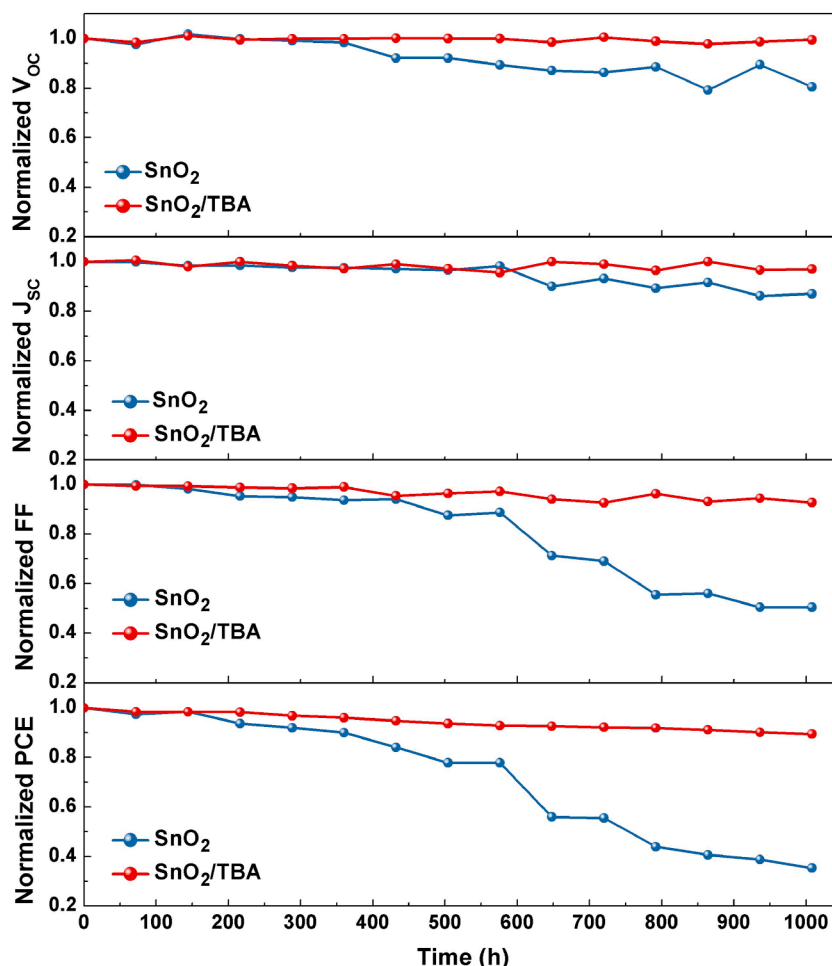

Fig. 6. Stability of J_{SC}, V_{OC}, FF, and PCE of the unencapsulated PSCs based on the unmodified and the TBA modified SnO_2 in ambient at ~ 20% RH.

ambient at ~ 20% RH, retained 88% after aging at ~ 50% RH for 200 h and 53% after aging under continuous illumination for 100 h. Our research provides a guidance for the design and development of multifunctional small molecule interface modification materials to improve the photovoltaic performance and long term stability of perovskite solar cells.

Declaration of Competing Interest

The authors declare that they have no known competing financial interests or personal relationships that could have appeared to influence the work reported in this paper.

Acknowledgements

Appendix A. Supplementary data

Supplementary data to this article can be found online at https://doi.org/10.1016/j.cej.2022.135134.

References

[1] A. Kojima, K. Teshima, Y. Shirai, T. Miyasaka, Organometal halide perovskites as visible-light sensitizers for photovoltaic cells, J. Am. Chem. Soc. 131 (17) (2009) 6050–6051, https://doi.org/10.1021/ja809598r.

[2] NREL, Best research-cell efficiencies. https://www.nrel.gov/pv/assets/pdfs/cell-pv-eff-emergingpv.202001042.pdf.

[3] H.-S. Kim, C.-R. Lee, J.-H. Im, K.-B. Lee, T. Moehl, A. Marchioro, S.-J. Moon, R. Humphry-Baker, J.-H. Yum, J.E. Moser, M. Gratzel, N.-G. Park, Lead iodide perovskite sensitized all-solid-state submicron thin film mesoscopic solar cell with efficiency exceeding 9%, Sci. Rep. 2 (2012) 591, https://doi.org/10.1038/srep00591.

[4] N.J. Jeon, J.H. Noh, W.S. Yang, Y.C. Kim, S. Ryu, J. Seo, S.I. Seok, Compositional engineering of perovskite materials for high-performance solar cells, Nature 517 (7535) (2015) 476–480, https://doi.org/10.1038/nature14133.

[5] Q.i. Jiang, Y. Zhao, X. Zhang, X. Yang, Y. Chen, Z. Chu, Q. Ye, X. Li, Z. Yin, J. You, Surface passivation of perovskite film for efficient solar cells, Nat. Photonics 13 (7) (2019) 460–466, https://doi.org/10.1038/s41566-019-0398-2.

[6] J.H. Noh, S.H. Im, J.H. Heo, T.N. Mandal, S.I. Seok, Chemical management for colorful, efficient, and stable inorganic-organic hybrid nanostructured solar cells, Nano Lett. 13 (4) (2013) 1764–1769, https://doi.org/10.1021/nl400349b.

[7] D.P. McMeekin, G. Sadoughi, W. Rehman, G.E. Eperon, M. Saliba, M.T. Hörantner, A. Haghighirad, N. Sakai, L. Korte, B. Rech, M.B. Johnston, L.M. Herz, H.J. Snaith, A mixed-cation lead mixed-halide perovskite absorber for tandem solar cells, Science 351 (2016) 151–155.

[8] S.D. Stranks, G.E. Eperon, G. Grancini, C. Menelaou, M.J.P. Alcocer, T. Leijtens, L. M. Herz, A. Petrozza, H.J. Snaith, Electron-hole diffusion lengths exceeding 1 micrometer in an organometal trihalide perovskite absorber, Science 342 (2013) 341–344.

[9] W.-J. Yin, T. Shi, Y. Yan, Unique properties of halide perovskites as possible origins of the superior solar cell performance, Adv. Mater. 26 (27) (2014) 4653–4658, https://doi.org/10.1002/adma.201306281.

[10] M. Liu, M.B. Johnston, H.J. Snaith, Efficient planar heterojunction perovskite solar cells by vapour deposition, Nature 501 (7467) (2013) 395–398, https://doi.org/10.1038/nature12509.

[11] C.Y. Xu, W. Hu, G. Wang, L. Niu, A.M. Elseman, L. Liao, Y. Yao, G. Xu, L. Luo, D. Liu, G. Zhou, P. Li, Q. Song, Coordinated optical matching of a texture interface made from demixing blended polymers for high-performance inverted perovskite solar cells, ACS Nano 14 (1) (2020) 196–203, https://doi.org/10.1021/acsnano.9b07594.10.1021/acsnano.9b07594.s001.

[12] G. Wang, L. Liao, L. Niu, L. Chen, W. Li, C. Xu, E. Mbeng, Y. Yao, D. Liu, Q. Song, Nuclei position-control and crystal growth-guidance on frozen substrates for high-performance perovskite solar cells, Nanoscale 11 (25) (2019) 12108–12115.

[13] Y. Yao, F. Lv, L. Luo, L. Liao, G. Wang, D. Liu, C. Xu, G. Zhou, X. Zhao, Q. Song, Highly efficient Sn-Pb perovskite solar cell and high-performance all-perovskite four-terminal tandem solar cell, Sol. RRL 4 (3) (2020) 1900396, https://doi.org/10.1002/solr.201900396.

[14] F. Ye, J. Ma, C. Chen, H. Wang, Y. Xu, S. Zhang, T.i. Wang, C. Tao, G. Fang, Roles of MACl in sequentially deposited bromine-free perovskite absorbers for efficient solar cells, Adv. Mater. 33 (3) (2021) 2007126, https://doi.org/10.1002/adma.202007126.

[15] X. Zhu, M. Du, J. Feng, H. Wang, Z. Xu, L. Wang, S. Zuo, C. Wang, Z. Wang, C. Zhang, X. Ren, S. Priya, D. Yang, S.(. Liu, High-efficiency perovskite solar cells with imidazolium-based ionic liquid for surface passivation and charge transport,

[16] H. Zhou, Q.i. Chen, G. Li, S. Luo, T.-B. Song, H.-S. Duan, Z. Hong, J. You, Y. Liu, Y. Yang, Interface engineering of highly efficient perovskite solar cells, Science 345 (6196) (2014) 542–546.

[17] C. Xu, Z. Liu, Q. Sun, E.-C. Lee, Morphology control of SnO₂ layer by solvent engineering for efficient perovskite solar cells, Solar Energy 214 (2021) 280–287, https://doi.org/10.1016/j.solener.2020.12.002.

[18] G. Wang, L.P. Liao, A.M. Elseman, Y.Q. Yao, C.Y. Lin, W. Hu, D.B. Liu, C.Y. Xu, G. D. Zhou, P. Li, L.J. Chen, J.J. Han, X. De Yang, R. Wu, X.i. Rao, Q.L. Song, An internally photoemitted hot carrier solar cell based on organic-inorganic perovskite, Nano Energy 68 (2020) 104383, https://doi.org/10.1016/j.nanoen.2019.104383.

[19] P. Chen, Z. Wang, S. Wang, M. Lyu, M. Hao, M. Ghasemi, M.u. Xiao, J.-H. Yun, Y. Bai, L. Wang, Luminescent europium-doped titania for efficiency and UV-stability enhancement of planar perovskite solar cells, Nano Energy 69 (2020) 104392, https://doi.org/10.1016/j.nanoen.2019.104392.

[20] J. Yang, B.D. Siempelkamp, E. Mosconi, F. De Angelis, T.L. Kelly, Origin of the thermal instability in CH₃NH₃PbI₃ thin films deposited on ZnO, Chem. Mater. 27 (12) (2015) 4229–4236, https://doi.org/10.1021/acs.chemmater.5b01598.

[21] X. Guo, J. Du, Z. Lin, J. Su, L. Feng, J. Zhang, Y. Hao, J. Chang, Enhanced efficiency and stability of planar perovskite solar cells using SnO₂:InCl₃ electron transport layer through synergetic doping and passivation approaches, Chem. Eng. J. 407 (2021) 127997, https://doi.org/10.1016/j.cej.2020.127997.

[22] L. Xiong, Y. Guo, J. Wen, H. Liu, G. Yang, P. Qin, G. Fang, Review on the application of SnO₂ in perovskite solar cells, Adv. Funct. Mater. 28 (35) (2018) 1802757, https://doi.org/10.1002/adfm.201802757.

[23] C. Altinkaya, E. Aydin, E. Ugur, F.H. Isikgor, A.S. Subbiah, M. De Bastiani, J. Liu, A. Babayigit, T.G. Allen, F. Laquai, A. Yildiz, S. De Wolf, Tin oxide electron-selective layers for efficient, stable, and scalable perovskite solar cells, Adv. Mater. 33 (15) (2021) 2005504, https://doi.org/10.1002/adma.202005504.

[24] J. Chen, J. Zhang, C. Huang, Z. Bi, X. Xu, H. Yu, SnO₂/2D-Bi₂O₂Se new hybrid electron transporting layer for efficient and stable perovskite solar cells, Chem. Eng. J. 410 (2021) 128436, https://doi.org/10.1016/j.cej.2021.128436.

[25] J.J. Yoo, G. Seo, M.R. Chua, T.G. Park, Y. Lu, F. Rotermund, Y.-K. Kim, C.S. Moon, N.J. Jeon, J.-P. Correa-Baena, V. Bulović, S.S. Shin, M.G. Bawendi, J. Seo, Efficient perovskite solar cells via improved carrier management, Nature 590 (7847) (2021) 587–593, https://doi.org/10.1038/s41586-021-03285-w.

[26] L. Kavan, L. Steier, M. Grätzel, Ultrathin buffer layers of SnO₂ by atomic layer deposition: perfect blocking function and thermal stability, J. Phys. Chem. C 121 (1) (2017) 342–350, https://doi.org/10.1021/acs.jpcc.6b0996510.1021/acs.jpcc.6b09965.s001.

[27] Q. Jiang, L. Zhang, H. Wang, X. Yang, J. Meng, H. Liu, Z. Yin, J. Wu, X. Zhang, J. You, Enhanced electron extraction using SnO₂ for high-efficiency planar-structure HC(NH₂)₂PbI₃-based perovskite solar cells, Nat. Energy 2 (2016) 16177, https://doi.org/10.1038/nenergy.2016.177.

[28] G.S. Han, J. Kim, S. Bae, S. Han, Y.J. Kim, O.Y. Gong, P. Lee, M.J. Ko, H.S. Jung, Spin-coating process for 10 cm × 10 cm perovskite solar modules enabled by self-assembly of SnO₂ nanocolloids, ACS Energy Lett. 4 (8) (2019) 1845–1851, https://doi.org/10.1021/acsenergylett.9b0095310.1021/acsenergylett.9b00953.s001.

[29] P. Wang, B. Chen, R. Li, S. Wang, N. Ren, Y. Li, S. Mazumdar, B. Shi, Y. Zhao, X. Zhang, Cobalt chloride hexahydrate assisted in reducing energy loss in perovskite solar cells with record open-circuit voltage of 1.20 V, ACS Energy Lett. 6 (6) (2021) 2121–2128, https://doi.org/10.1021/acsenergylett.1c0044310.1021/acsenergylett.1c00443.s001.

[30] D. Yang, R. Yang, K. Wang, C. Wu, X. Zhu, J. Feng, X. Ren, G. Fang, S. Priya, S. F. Liu, High efficiency planar-type perovskite solar cells with negligible hysteresis using EDTA-complexed SnO₂, Nat. Commun. 9 (2018) 3239, https://doi.org/10.1038/s41467-018-05760-x.

[31] Z. Dai, S.K. Yadavalli, M. Chen, A. Abbaspourtamijani, Y. Qi, N.P. Padture, Interfacial toughening with self-assembled monolayers enhances perovskite solar cell reliability, Science 372 (2021) 618–622.

[32] G. Tumen-Ulzii, T. Matsushima, D. Klotz, M.R. Leyden, P. Wang, C. Qin, J.-W. Lee, S.-J. Lee, Y. Yang, C. Adachi, Hysteresis-less and stable perovskite solar cells with a self-assembled monolayer, Commun. Mater. 1 (2020) 31, https://doi.org/10.1038/s43246-020-0028-z.

[33] Z. Liu, L. Qiu, L.K. Ono, S. He, Z. Hu, M. Jiang, G. Tong, Z. Wu, Y. Jiang, D.-Y. Son, Y. Dang, S. Kazaoui, Y. Qi, A holistic approach to interface stabilization for efficient perovskite solar modules with over 2,000-hour operational stability, Nat. Energy 5 (8) (2020) 596–604, https://doi.org/10.1038/s41560-020-0653-2.

[34] H. Xia, X. Li, J. Zhou, B. Wang, Y. Chu, Y. Li, G. Wu, D. Zhang, B. Xue, X. Zhang, Y. Hu, H. Zhou, Y. Zhang, Interfacial chemical bridge constructed by zwitterionic sulfamic acid for efficient and stable perovskite solar cells, ACS Appl. Energy Mater. 3 (4) (2020) 3186–3192, https://doi.org/10.1021/acsaem.0c0013710.1021/acsaem.0c00137.s001.

[35] S.P. Dunfield, L. Bliss, F. Zhang, J.M. Luther, K. Zhu, M.F.A.M. Hest, M.O. Reese, J. J. Berry, From defects to degradation: a mechanistic understanding of degradation in perovskite solar cell devices and modules, Adv. Energy Mater. 10 (26) (2020) 1904054, https://doi.org/10.1002/aenm.201904054.

[36] B. Liu, H. Bi, D. He, L.e. Bai, W. Wang, H. Yuan, Q. Song, P. Su, Z. Zang, T. Zhou, J. Chen, Interfacial defect passivation and stress release via multi-active-site ligand anchoring enables efficient and stable methylammonium-free perovskite solar cells, ACS Energy Lett. 6 (7) (2021) 2526–2538, https://doi.org/10.1021/acsenergylett.1c0079410.1021/acsenergylett.1c00794.s001.

[37] J. Wu, Y. Cui, B. Yu, K. Liu, Y. Li, H. Li, J. Shi, H. Wu, Y. Luo, D. Li, Q. Meng, A simple way to simultaneously release the interface stress and realize the inner

encapsulation for highly efficient and stable perovskite solar cells, Adv. Funct. Mater. 29 (49) (2019) 1905336, https://doi.org/10.1002/adfm.201905336.

[38] L. Zuo, Q.i. Chen, N. De Marco, Y.-T. Hsieh, H. Chen, P. Sun, S.-Y. Chang, H. Zhao, S. Dong, Y. Yang, Tailoring the interfacial chemical interaction for high-efficiency perovskite solar cells, Nano Lett. 17 (1) (2017) 269–275, https://doi.org/10.1021/acs.nanolett.6b0401510.1021/acs.nanolett.6b04015.s001.

[39] L. Zuo, Z. Gu, T. Ye, W. Fu, G. Wu, H. Li, H. Chen, Enhanced photovoltaic performance of CH₃NH₃PbI₃ perovskite solar cells through interfacial engineering using self-assembling monolayer, J. Am. Chem. Soc. 137 (7) (2015) 2674–2679, https://doi.org/10.1021/ja512518r.

[40] Y. Sun, J. Zhang, H. Yu, J. Wang, C. Huang, J. Huang, Mechanism of bifunctional p-amino benzenesulfonic acid modified interface in perovskite solar cells, Chem. Eng. J. 420 (2021) 129579, https://doi.org/10.1016/j.cej.2021.129579.

[41] H. Bi, B. Liu, D. He, L.e. Bai, W. Wang, Z. Zang, J. Chen, Interfacial defect passivation and stress release by multifunctional KPF₆ modification for planar perovskite solar cells with enhanced efficiency and stability, Chem. Eng. J. 418 (2021) 129375, https://doi.org/10.1016/j.cej.2021.129375.

[42] M. Hou, H. Zhang, Z.e. Wang, Y. Xia, Y. Chen, W. Huang, Enhancing efficiency and stability of perovskite solar cells via a self-assembled dopamine interfacial layer, ACS Appl. Mater. Interfaces 10 (36) (2018) 30607–30613, https://doi.org/10.1021/acsami.8b1033210.1021/acsami.8b10332.s001.

[43] J. Chen, X. Zhao, S.-G. Kim, N.-G. Park, Multifunctional chemical linker imidazoleacetic acid hydrochloride for 21% efficient and stable planar perovskite solar cells, Adv. Mater. 31 (39) (2019) 1902902, https://doi.org/10.1002/adma.201902902.

[44] W. Zhang, X. Li, X. Feng, X. Zhao, J. Fang, A conjugated ligand interfacial modifier for enhancing efficiency and operational stability of planar perovskite solar cells, Chem. Eng. J. 412 (2021) 128680, https://doi.org/10.1016/j.cej.2021.128680.

[45] R. Yuan, B. Cai, Y. Lv, X. Gao, J. Gu, Z. Fan, X. Liu, C. Yang, M. Liu, W.-H. Zhang, Boosted charge extraction of NbOₓ-enveloped SnO₂ nanocrystals enables 24% efficient planar perovskite solar cells, Energy Environ. Sci. 14 (9) (2021) 5074–5083.

[46] X. Zhao, J. Dong, D. Wu, J. Zhou, J. Feng, Y. Yao, C.Y. Xu, X. Yang, X. Tang, Q. Song, Efficient and stable perovskite solar cells achieved by using bifunctional interfacial materials to modify SnO₂ and MAPbI₃₋ₓClₓ simultaneously, ACS Appl. Energy Mater. 4 (4) (2021) 3794–3802, https://doi.org/10.1021/acsaem.1c0019210.1021/acsaem.1c00192.s001.

[47] J. Zhang, H. Yu, Reduced energy loss enabled by thiophene-based self-assembled monolayer for high performance and stability perovskite solar cells, J. Mater. Chem. A 9 (2021) 4138–4149, https://doi.org/10.1039/d0ta10270a.

[48] W. Lin, Y.F. Zhang, Y. Li, Y. Chen, J.Q. Li, First principle studies on the geometry and electronic structures of the SnO₂ (110) surface, Acta Phys. -Chim. Sin. 22 (2006) 76–81, https://doi.org/10.3866/pku.Whxb20060115.

[49] C. Xu, Y. Yao, G. Wang, J. Dong, G. Xu, Y. Zhong, D. Lu, X. Zhao, D. Liu, G. Zhou, X. Yang, P. Li, L. Chen, Q. Song, Self-woven monolayer polyionic mesh to achieve highly efficient and stable inverted perovskite solar cells, Chem. Eng. J. 428 (2022) 132074, https://doi.org/10.1016/j.cej.2021.132074.

[50] W. Deng, F. Li, J. Li, M. Wang, Y. Hu, M. Liu, Anti-solvent free fabrication of FA-based perovskite at low temperature towards to high performance flexible perovskite solar cells, Nano Energy 70 (2020) 104505, https://doi.org/10.1016/j.nanoen.2020.104505.

[51] J. Zhuang, P. Mao, Y. Luan, N. Chen, X. Cao, G. Niu, F. Jia, F. Wang, S. Cao, J. Wang, Rubidium fluoride modified SnO₂ for planar n-i-p perovskite solar cells, Adv. Funct. Mater. 31 (17) (2021) 2010385, https://doi.org/10.1002/adfm.202010385.

[52] H. Bi, X. Zuo, B. Liu, D. He, L.e. Bai, W. Wang, X. Li, Z. Xiao, K. Sun, Q. Song, Z. Zang, J. Chen, Multifunctional organic ammonium salt modified SnO₂ nanoparticles toward efficient and stable planar perovskite solar cells, J. Mater. Chem. A 9 (7) (2021) 3940–3951.

[53] Q.L. Song, H.R. Wu, X.M. Ding, X.Y. Hou, F.Y. Li, Z.G. Zhou, Exciton dissociation at the indium tin oxide-N, N′-Bis(naphthalen-1-yl)-N, N′-bis(phenyl) benzidine interface: A transient photovoltage study, Appl. Phys. Lett. 88 (23) (2006) 232101, https://doi.org/10.1063/1.2209203.